Parametric and non-parametric statistical approaches to the determination of paleostress from dilatant fractures: Application to an Early Miocene dike swarm in central Japan

Katsushi Sato[a], Atsushi Yamaji[a], Satoshi Tonai[a,b]

[a] *Division of Earth and Planetary Sciences, Graduate School of Science, Kyoto University, Kyoto 606-8502, Japan*
[b] *Present address: Department of Applied Science, Faculty of Science, Kochi University, Kochi 780-8520, Japan*

Abstract

Several methods have been proposed for determining paleostress states from orientations of dilatant fractures such as dikes and veins. Recently a stochastic inversion method was invented to objectively estimate the principal stress axes and the stress ratio. Whether a fracture is dilated or not is controlled by the balance of the fluid pressure and the normal stress acting on it. The magnitude of normal stress depends on the fracture orientation, which causes anisotropic orientation distribution of dilatant fractures. The inversion method assumes that the orientation distribution of fractures can be approximated by a Bingham distribution, an exponential probability distribution on the unit sphere, of which symmetric axes are interpreted as the principal stress axes. However, it is unknown if the exponential type of distribution function is suitable or not. Here, we examine the distribution functions and propose two improved methods. One method uses the shifted power-law function as the shape of probability distribution, which is more

flexible than the Bingham distribution and is applicable to various shapes of orientation distributions. Furthermore, an index of the driving fluid pressure can be estimated with a confidence interval. The other is a non-parametric (distribution-free) method, which can avoid the a priori assumption on the shape of distribution function without significantly losing accuracy or precision. The new methods were applied to an Early Miocene dike swarm formed during the back-arc opening of the Japan Sea. A normal-faulting stress regime with the minimum principal stress axis trending roughly perpendicular to the arc was obtained from the dikes. A moderately high stress ratio and a high fluid pressure were also estimated.
Keywords: dilatant fracture, dike swarm, tectonic stress, inversion, non-parametric statistics

1. Introduction

Orientations of dilatant fractures such as dikes and mineral veins provide clues to the tectonic paleostress under the influence of crustal fluid. Extension fractures have been thought to be perpendicular to the regional minimum compressive principal stress axis (e.g. Anderson, 1951; Nakamura, 1977). However, natural fractures have variations in their orientations to some extent. As is mentioned below, we can explain some types of such variations without assuming spatiotemporal changes of tectonic stress states, and the variations carry information on the other parameters of stress tensors.

Delaney et al. (1986) formulated the criterion for re-opening of pre-existing fractures as

$$P_{\mathrm{f}} \geq \sigma_{\mathrm{n}}, \tag{1}$$

where P_{f} is the pressure of the fluid which makes dikes or veins, and σ_{n} is the tectonic normal stress acting on the fracture surface (Fig. 1). This criterion neglects tensile strength of pre-existing fracture. Even in a uniform and constant stress field the magnitude of normal stress acting on a fracture varies with its orientation (Fig. 2). Then the criterion (Eq. 1) restricts the range of orientations of dilatant fractures.

Jolly and Sanderson (1997) proposed a graphical method to determine stress conditions from the range of fracture orientations (Fig. 3a). Let σ_1, σ_2 and σ_3 be the maximum, intermediate and minimum compressive principal stresses. The feasible range of fracture poles should be centered by σ_3-axis. If the fluid pressure satisfies $P_{\mathrm{f}} < \sigma_1$, there is a blank region centered by σ_1-axis. After specifying σ_3- and σ_1-axes as the orientations with the maximum and minimum frequencies of fracture poles, σ_2-axis can be determined so as to be perpendicular to both σ_1- and σ_3-axes. The determination of principal axes can be achieved numerically by utilizing eigenvectors of orientation-distribution tensor (Scheidegger, 1965; Woodcock, 1977). The feasible range of fracture poles is not always concentric around σ_3-axis but tends to extend broader toward σ_2-axis than toward σ_1-axis. Jolly and Sanderson (1997) proposed to determine the stress ratio $\Phi = (\sigma_2 - \sigma_3)/(\sigma_1 - \sigma_3)$ from the geometry of feasible range in relation to the fluid pressure level (Fig. 3a). Φ ranges from 0 (axial compression) to 1 (axial tension), which represents the shape of stress ellipsoid. Consequently, the purpose of an analysis of dilatant fractures is to constrain the combination of the three principal stress axes and the stress ratio. These independent four variables of a stress tensor are mathematically expressed by a normalized symmetric matrix, which is called

'reduced stress tensor' in the methodology of stress tensor inversion from fault-slip data (e.g. Angelier, 1989). In this study, σ_1 and σ_3 are normalized to be 1 and 0, respectively.

Although the Jolly and Sanderson's method has been applied to natural dilatant fractures (e.g. Andre et al., 2001; Mazzarini and Isola, 2007), there is a difficulty in the recognition of the border of feasible region on stereograms (Fig. 3a). In many cases the frequency of poles to fractures gradually diminishes toward the border. We have proposed that the problem can be solved by assuming that the variation of frequency reflects the difference of tectonic normal stress arising from the difference of fracture orientation (Fig. 2). Our method fits a Bingham distribution (Bingham, 1974), an exponential probability distribution on sphere, to the orientation distribution of poles to fractures (Fig. 3b). The Bingham stochastic model carries parameters which can be interpreted as those of a reduced stress tensor. The symmetric axes of the optimized Bingham distribution represents the principal stress axes. The anisotropy of distribution on sphere indicates the stress ratio (Fig. 2). Our approach seemed to have succeeded in analyzing epithermal quartz vein swarm in an area in southern Japan and a normal-faulting tectonic stress was obtained.

However, the validity of the exponential stochastic model has not been examined. There possibly is an orientation distribution which is not suitable for the approximation by an exponential function. This study proposes two improved methods. One employs a stochastic model of shifted power-law function which has a larger degrees of freedom than the exponential function. The new function is expected to express various types of decreasing function

flexibly (Fig. 3c). The other modified method is non-parametric without any stochastic model. This method searches for a stress state which optimizes the rank correlation coefficient between fracture frequencies and normal stress magnitudes. Its advantage is in the exclusion of a priori assumption on the shape of orientation distribution function. For the purpose of comparing the methods, this paper presents analyses of simulated and natural datasets.

2. Method

Let $\boldsymbol{\sigma}$ and $\boldsymbol{\sigma}_0$ be a stress tensor and its expression in the principal coordinate system, respectively. They can be written as

$$\boldsymbol{\sigma}_0 = \begin{pmatrix} 1 & 0 & 0 \\ 0 & \Phi & 0 \\ 0 & 0 & 0 \end{pmatrix}. \tag{2}$$

and

$$\boldsymbol{\sigma} = Q^{\mathrm{T}} \boldsymbol{\sigma}_0 Q, \tag{3}$$

where Q is the orthogonal matrix as the coordinate rotation operator and the superscript T denotes transpose of matrix. When σ_1 and σ_3 are normalized to be 1 and 0, σ_2 corresponds to the stress ratio Φ by definition. Given a unit normal of fracture plane $\vec{v} = (x, y, z)^{\mathrm{T}}$, where x, y and z are the Cartesian coordinates in the physical space, and its expression in the principal coordinate system $\vec{v}_0 = (x_0, y_0, z_0)^{\mathrm{T}}$, the magnitude of normal stress is calculated to be

$$\sigma_{\mathrm{n}}(\vec{v}; \boldsymbol{\sigma}) = \vec{v}^{\mathrm{T}} \boldsymbol{\sigma} \vec{v} = \vec{v}_0^{\mathrm{T}} \boldsymbol{\sigma}_0 \vec{v}_0 = x_0^2 + \Phi y_0^2. \tag{4}$$

Our assumption is that the probability of dilatant fracturing to have an orientation $\vec{v}$ is written as a monotonic decreasing function of

$$P\left(\vec{v};\boldsymbol{\sigma}\right) = f\left(\sigma_{\mathrm{n}}\left(\vec{v};\boldsymbol{\sigma}\right)\right)\mathrm{d}A, \tag{5}$$

where f is an arbitrary decreasing function and dA is the area element of the unit sphere on which the end point of $\vec{v}$ lies. The nature of stress tensor inversion methods discussed in this paper is the optimization of $\boldsymbol{\sigma}$ in Eq. (5) so as to fit P to the observed frequency distribution of fracture orientations $(\vec{v})$. The formula of f can be freely chosen and three methods are defined and examined below.

2.1. Bingham method

Yamaji et al. (2010) used the Bingham distribution (Bingham, 1974) for its simplicity and resemblance to the two-dimensional normal distribution. The distribution can express a variety of concentrations of spherical axial data including a point concentration and a concentration along girdle. The probability density function involves two concentration parameters κ_1 and κ_2 $(\kappa_1 \leq \kappa_2 \leq 0)$ in two orthogonal principal directions,

$$\begin{aligned} f_{\mathrm{B}}\left(\vec{v};\boldsymbol{\sigma}\right) &= A_{\mathrm{B}}\exp\left(\kappa_1 x_0^2 + \kappa_2 y_0^2\right) \\ &= A_{\mathrm{B}}\exp\left\{\kappa_1\left(x_0^2 + \Phi y_0^2\right)\right\} \\ &= A_{\mathrm{B}}\exp\left(\kappa_1\sigma_{\mathrm{n}}\right), \end{aligned} \tag{6}$$

where $\Phi = \kappa_2/\kappa_1$ and Eq. (4) was employed. The normalization constant A_{B} is set so as to satisfy $\int_{S_3} f_{\mathrm{B}} dA = 1$, where S_3 is the unit sphere. The principal stress axes coincide with principal axes of Bingham distribution; the maximum concentration at σ_3-axis. When $\kappa_1 = \kappa_2$, the probability is

concentric around this axis; and when $\kappa_2 = 0$, the concentration becomes girdle-type along the great circle connecting σ_3- and σ_2-axes.

The unknowns to be determined in an inversion analysis are the reduced stress tensor and the concentration parameter κ_1. Accordingly, the degrees of freedom of the Bingham model is five. Given a set of fracture orientations $\vec{v}_i$ $(i = 1, \cdots, N)$, where N is the number of fracture, the sum of logarithmic likelihood is defined as

$$L_{\mathrm{B}}(\boldsymbol{\sigma}, \kappa_1) = \sum_{i=1}^{N} \ln f_{\mathrm{B}}(\vec{v}_i; \boldsymbol{\sigma}) \, \mathrm{d}A. \tag{7}$$

The unknown parameters are optimized by maximizing L_{B}.

The optimization is performed by the simplex method (Nelder and Mead, 1965). This method requires the initial values of unknown parameters, which are chosen according to the eigenanalysis of orientation-distribution tensor,

$$T = \frac{1}{N} \sum_{i=1}^{N} \vec{v}_i \vec{v}_i^{\mathrm{T}}. \tag{8}$$

Let T_1, T_2 and T_3 be the maximum, intermediate and minimum eigenvalues of T. The eigenvectors corresponding to T_1, T_2 and T_3 are assigned to initial orientations of σ_3-, σ_2- and σ_1-axes, respectively. The initial estimates of the concentration parameters are set as $\kappa_1 = -1/(2T_1)$ and $\kappa_2 = -1/(2T_2)$, accordingly $\Phi = T_1/T_2$.

2.2. Shifted power-law method

In the pioneering work of Jolly and Sanderson (1997), a distribution of dilatant fracture poles was expected to have a clear limit when it is visualized on a stereogram (Fig. 3a). If the frequency of fracture poles has a step-wise

decrease, one can easily recognize the limit. However, it is not easy for the Bingham distribution model to express a step-wise change of frequency. Here we introduce another type of probability distribution, which we call shifted power-law distribution,

$$f_{\mathrm{p}}\left(\vec{v};\boldsymbol{\sigma}\right)=\begin{cases} A_{\mathrm{p}}\left(\lambda-\sigma_{\mathrm{n}}\right)^{n} & \left(\sigma_{\mathrm{n}}\leq\lambda\right) \\ 0 & \left(\sigma_{\mathrm{n}}>\lambda\right), \end{cases} \tag{9}$$

where A_{p}, λ and n are constants. The normalization factor A_{p} is chosen so as to satisfy $\int_{S_3} f_{\mathrm{p}} dA = 1$. The parameter λ corresponds to the fluid pressure level; if the tectonic normal stress exceeds this value, a fracture is not supposed to open (Eq. 1). Since magnitude of stress are normalized in our formulation, λ is the nondimensionalized fluid pressure, $\lambda = (P_{\mathrm{f}} - \sigma_3)/(\sigma_1 - \sigma_3)$. The exponent n allows the function to flexibly express various shapes of decreasing functions (Fig. 4). Not only a convex shape like an exponential function ($n > 1$) but also a linear ($n = 1$) and a concave shape ($0 < n < 1$) are included in this model.

The degrees of freedom of shifted power-law model is six; four for the parameters of a reduced stress tensor and two for the nondimensionalized fluid pressure λ and the exponent n. They are optimized by maximizing the sum of logarithmic likelihood,

$$L_{\mathrm{p}}\left(\boldsymbol{\sigma},\lambda,n\right)=\sum_{i=1}^{N}\ln f_{\mathrm{p}}\left(\vec{v}_i;\boldsymbol{\sigma}\right)\mathrm{d}A. \tag{10}$$

The simplex method is employed for optimization. The initial solution of principal stress orientations are given as eigenvectors of the orientation-distribution tensor (Eq. 8). The initial values of the other parameters are set as $\Phi = T_1/T_2$, $\lambda = 1$ and $n = 1$.

2.3. Non-parametric method

The above-mentioned two methods (Sections 2.1 and 2.2) make a priori assumptions on the shape of probability distribution functions in the stochastic models. For the purpose of excluding this assumption, we propose a non-parametric approach assuming only the monotonic decrease of frequency against normal stress magnitude:

$$\text{If} \quad \sigma_{\mathrm{n}}(\vec{v}_i) > \sigma_{\mathrm{n}}(\vec{v}_j), \quad \text{then} \quad f(\vec{v}_i) \leq f(\vec{v}_j), \tag{11}$$

where $\vec{v}_i$ and $\vec{v}_j$ are arbitrary unit normals to fractures, and $f(\vec{v})$ is the frequency of fractures around $\vec{v}$. As the objective function of inversion analysis, we introduce Spearman's rank correlation coefficient (Spearman, 1904), which is not affected by the gradient of decreasing function and can quantify to what extent the relationship of Eq. (11) is satisfied.

When we have a set of fracture orientations, frequency of their poles are estimated at 500 grid points uniformly distributed on the unit sphere. The grid points were generated according to the method of Rakhmanov et al. (1994). Similarly to the way of drawing density diagram on stereogram, the probability density of the Fisher distribution (Fisher, 1953) with the concentration parameter set to 100 is assigned to each datum point and summed up for all data to obtain the frequencies at the grid points. If an arbitrary reduced stress tensor is given, normal stress magnitudes on the fractures corresponding to the grid points can be calculated immediately. Let D_i be the difference between the rank of normal stress magnitude in ascending order and that of frequency of fracture normals in descending order for ith grid point among all grid points (Fig. 5). Spearman's rank correlation

coefficient is defined as

$$\rho = 1 - \frac{6 \sum_{i=1}^{N_\mathrm{G}} D_i^2}{N_\mathrm{G}(N_\mathrm{G}^2 - 1)}, \tag{12}$$

where N_G is the number of grid points. The value of ρ ranges from -1 (negative correlation) to 1 (positive correlation).

Our task is to search for an optimal reduced stress tensor to maximize the rank correlation coefficient. The degrees of freedom in this non-parametric method is four, just for the unknown parameters of reduced stress tensor. Note that we use the word 'non-parametric', and this method is also parametric as for stress model. The optimization is again made by the simplex method. The initial solution of reduced stress tensor is given by the orientation-distribution tensor similarly to the Bingham method and the shifted power-law method.

2.4. Confidence region

The confidence regions of optimal solutions are estimated by the bootstrap technique for all the three methods. In a trial of bootstrap process, N data are resampled with replacement from the original N data. Then the resampled dataset is analyzed to obtain a bootstrap solution. This trial is repeated N_B times. The number of bootstrap solutions N_B should satisfy $N_\mathrm{B} \gg N$ and it is set to 1000 in the following analyses.

The bootstrap solutions are ranked according to their distances to the optimal solution for the original dataset in ascending order. The distance is measured by the stress difference (Orife and Lisle, 2003; Yamaji and Sato, 2006), which evaluates the differences between reduced stress tensors. The lowest (distant) 5% of bootstrap solutions are excluded and the spread of

the rest 95%, 950 solutions in this case, is interpreted as the 95% confidence region. The outline of distribution of 950 solutions are drawn as to principal stress orientations and the other parameters optimized in inversion analyses to visualize the confidence regions.

3. Test

In this section the three methods are compared through analyses of two artificial fracture orientation datasets with known stress solutions and a natural dataset acquired by Yamaji et al. (2010).

3.1. Test 1: Exponential frequency distribution

Artificial 100 fracture orientations were randomly generated by using acceptance-rejection method so that their poles obey a Bingham distribution (Fig. 6a). The following principal stress axes were assigned, σ_1: 000/00, σ_2: 090/00 and σ_3: 000/90 (reverse-faulting regime). The concentration parameters were set as $\kappa_1 = -6$ and $\kappa_2 = -3$. Therefore, the assumed stress ratio is $\Phi = \kappa_2/\kappa_1 = 0.5$. The Bingham method is of course expected to work better than the other two methods in both accuracy and precision for this dataset.

The results of analyses by the three methods are shown in Fig. 7. The 95% confidence regions of the principal stress axes determined by all three methods include the correct orientations, although the deviations of optimal axes are up to 15° (Fig. 7a). The areas of confidence regions of the Bingham method are smaller, i.e., the precision is higher, than those of the other two methods. Though the precision of the non-parametric method is the lowest, the differences of precisions among methods are not so large.

Fig. 7b shows the other parameters optimized in the analyses and their confidence intervals. The assumed stress ratio $\Phi = 0.5$ is within the confidence regions for all three methods. The three methods roughly have similar precisions. However, the optimal stress ratios of the shifted power-law and the non-parametric methods slightly deviate from the correct solution: 0.55 and 0.60, respectively. The concentration parameters were also determined successfully through the Bingham method: $\kappa_1 = -6.1 + 1.7/ - 3.6$ and $\kappa_2 = -3.2 + 1.3/ - 1.7$.

Fig. 7c includes the Mohr's diagrams (the first row) and frequencies of normal stress magnitudes (the second row) calculated according to the optimal reduced stress tensors. The frequencies in the second row were calculated through a correction as follows. If the isovalue line of a σ_{n} value is long on the unit sphere (Fig. 2), we should observe a larger number of fractures having the value of normal stress. This geometrical effect is removed by dividing the frequencies by the areas on the unit sphere corresponding to the ranges of σ_{n}. Appendix A explains the calculation of the area which depends on the stress ratio. The corrected frequencies were normalized as a probability density. The optimized functions of the Bingham and shifted power-law methods are also shown in the second row of Fig. 7c. Note that the frequencies of fractures roughly decrease against the normal stress magnitude in all three results.

The optimal exponent of the shifted power-law method is $n = 6.5 + 155.5/ - 6.3$ which gives a convex shape of distribution function so as to simulate the exponential decrease of the assumed Bingham distribution (Figs. 7b and 7c). Since a large n (> 1) gives a distribution function asymptotic to

the horizontal axis, the nondimensionalized fluid pressure has an extremely large uncertainty interval; $\lambda = 1.4 + 253/-1.1$. This result implies that when n is large, we cannot determine the nondimensionalized fluid pressure well.

The non-parametric method produces only the parameters of reduced stress tensors (Fig. 7b). Spearman's rank correlation coefficient for the optimal stress solution was $\rho = 0.892$ which indicates a strong positive correlation. Note that the optimal reduced stress tensor of the non-parametric method was almost equivalent to those of parametric methods.

3.2. Test 2: Step-wise frequency distribution

Another artificial fracture dataset was generated so that its orientational frequency obeys a step-wise distribution function (Fig. 6b). A stress state with σ_1-axis at 090/00, σ_2-axis at 000/00, σ_3-axis at 000/90 (reverse-faulting regime) and a stress ratio $\Phi = 0.3$ was assigned. The assumed distribution can be described by the shifted power-law function with $n = 0$ and $\lambda = 0.6$, which means a constant frequency for $0 \leq \sigma_{\mathrm{n}} \leq 0.6$ and zero frequency for $0.6 < \sigma_{\mathrm{n}} \leq 1$. The acceptance-rejection method was used to generate the artificial fracture orientations obeying this distribution. The shifted power-law method is expected to work better than the other two.

The results of analyses are shown in Fig. 8. The principal stress axes were correctly determined by all three methods (Fig. 8a). Note that the orientations of σ_2- and σ_3-axes were poorly determined because of the assumed small stress ratio (nearly axial compressional stress). As for the precision of σ_1 axis, the shifted power-law method was the highest.

The optimal stress ratios of all three methods have confidence regions including the correct value, $\Phi = 0.3$ (Fig. 8b). However, the optimal values

of Bingham and non-parametric methods are largely deviated ($\Phi = 0.15 + 0.22/-0.13$ and $\Phi = 0.49 + 0.18/-0.48$, respectively), while that of shifted power-law method is almost exact ($\Phi = 0.28 + 0.31/-0.28$).

The shifted power-law method succeeded in determining the other parameters $n = 0.028 + 0.465/-0.028$ (assumed to be 0) and $\lambda = 0.586 + 0.134/-0.084$ (assumed to be 0.6). The optimized stochastic model is approximately step-wise (Fig. 8c). We can also see that the optimized Bingham model has difficulties in simulating the step-wise frequency distribution, which may cause the deviation of optimal stress ratio. The optimized rank correlation coefficient of the non-parametric method was $\rho = 0.736$. This test demonstrated that the accuracy of principal stress axes is relatively independent of the choice of method, while the stress ratio and the other parameters are significantly affected.

3.3. Test 3: A natural vein swarm

A natural vein swarm investigated by Yamaji et al. (2010) was re-analyzed by the new methods. The Pliocene epithermal quartz veins are distributed in the Hashima area, southern Japan. Yamaji et al. (2010) acquired 233 vein orientations (Fig. 6c), which were analyzed by the Bingham method and a normal-faulting stress was detected.

Fig. 9 shows the results of analyses in this study. There is no significant difference in the optimal reduced stresses calculated by the three methods, except that the precision of the Bingham method is slightly higher. The frequency of veins drastically decreases against the increase of tectonic normal stress (Fig. 9c) and the Bingham model appears to be suited for this data. A large exponent $n = 5 + 206.2/-4.0$ of the shifted power-law model

was chosen to simulate the quasi-exponential distribution and the optimized models of the two parametric methods are very similar. At least in this case the choice of stochastic models does not affect the result as Yamaji et al. (2010) pointed out. The non-parametric method, of which optimized rank correlation coefficient was $\rho = 0.946$, is also worked well. It achieved the equivalent precisions to the two parametric methods without assumption on the stochastic model. Consequently, this natural example showed that all the three methods are usable to infer tectonic stress from a natural fracture orientations which has a simple frequency distribution against normal stress.

Yamaji et al. (2010) estimated the nondimensionalized fluid pressure level at $\lambda = 0.55$ by picking up the maximum normal stress among all the veins. However, because of the nature of the quasi-exponential distribution which is asymptotic to zero frequency, the confidence region of the nondimensionalized fluid pressure determined by the shifted power-law method is large: $\lambda = 0.90 + 24.58/ - 0.50$. It is therefore difficult to estimate λ from this vein swarm.

4. Application to Miocene dike swarm

4.1. Geological setting

We applied the new inversion methods to a dike swarm in the Tsuruga Bay area, back-arc side of central Japan (Fig. 10a). The host rock of the dikes is a late Paleozoic to early Mesozoic accretionary complex called the Mino terrain which is composed of mélange of sandstones and mudstones, siliceous mudstone, limestone, chert and basalt (Wakita et al., 1992). Lower Miocene lava and pyroclastic rocks cover them. There also occur Lower

Miocene andesitic dikes intruded into the basement (Fig. 10b). A K-Ar age of 19 Ma was obtained from one of the andesitic dike by Hoshi and Takagawa (2009).

Hoshi and Takagawa (2009) measured the orientations of 47 dikes and found the cluster of dike poles in the SE-quadrant, thereby a NW-SE trending σ_{Hmin} was inferred. They did not determined the stress regime at the time of intrusion, but they thought on the basis of this arc-parallel trend and the age that the swarm represents the extensional stress during the backarc opening in the Japan Sea.

The purpose of the present analysis is to refine the paleostress estimation by Hoshi and Takagawa (2009) by determining the stress regime, stress ratio and nondimensionalized fluid pressure.

4.2. Data

We collected 100 orientations of andesitic dikes from outcrops along the coast of about 15 km long (Fig. 10a). Most of the dikes are roughly planar and their widths range from 5 cm to 10 m. If a dike is sinuous, the general attitude of the boundary between the dike and the host rock was adopted. Although the opening directions of dikes are rarely identified, there is no slicken striation on the surfaces of dikes and no shear deformation parallel to a dike was recognized. A few jigsaw structures evidence the opening directions perpendicular to the dikes (Fig. 10c).

Fig. 6d shows the measured orientations of the dikes. They have diverse orientations while a concentration of their poles is found at NW-SE. It should be noted that there is obviously an elliptic vacant area around the vertical axis. This implies that the outline of the ellipse corresponds to the boundary

between the orientations for which the condition $P_{\mathrm{f}} \geq \sigma_{\mathrm{n}}$ is satisfied or not (Jolly and Sanderson, 1997). The host rock of the study area is dominated by mélange of sandstones and mudstones which has fractures of various orientations. Therefore, re-opening of pre-existing fractures appears to be likely to occur as is assumed by Jolly and Sanderson (1997).

4.3. Result of analyses

Similarly to Section 3, the dikes in the Tsuruga Bay area were analyzed by the three methods. The three optimal reduced stress tensors are roughly similar and are normal-faulting regimes (Fig. 11). Nearly vertical σ_1-axis, NE-SW trending σ_2-axis, NW-SE trending σ_3-axis and a moderately high stress ratio ($\Phi \approx 0.7$) were obtained. Differences were found in precision. The precision of the shifted power-law method is superior to the other two.

The exponent of the shifted power-law model was determined as $n = 0.84{+}18.0/{-}0.84$ indicating a linear to slightly concave shape (Fig. 11c). The nondimensionalized fluid pressure is $\lambda = 0.76{+}3.59/{-}0.20$, which defines the horizontal intercept of the model function. This shape appears to be suited to the data distribution which has an abrupt extinction at $\sigma_{\mathrm{n}} = \lambda$, while the long tail of the Bingham model cannot express it. The non-parametric method resulted in the optimized rank correlation coefficient of $\rho = 0.802$. The precisions of the Bingham and the non-parametric methods are comparable.

4.4. Comparison to the Jolly-Sanderson method

We applied the graphical method of Jolly and Sanderson (1997) to the dikes for comparison to the present methods (Fig 6d). The principal stress axes were supposed to coincide with the eigenvectors of orientation-distribution

tensor. The vacant area was roughly centered by σ_1-axis. Then the size of the vacant area is measured along the principal planes; $\theta_3 = 60°$ toward σ_2-axis and $\theta_2 = 30°$ toward σ_3-axis. According to Jolly and Sanderson (1997) and Andre et al. (2001), the stress ratio was calculated:

$$\Phi = 1 - \frac{\cos 2\theta_2 - 1}{\cos 2\theta_3 - 1} \approx 0.67. \tag{13}$$

As for this dike swarm, the vacant area can be clearly recognized so that this ratio does not have a significant difference to those by the inversion analyses.

5. Discussion

Through the tests using artificial and natural fracture data, the present all three methods were confirmed to be generally useful to determine a reduced stress tensor from an dilatant fracture dataset according to the assumption that the frequency of fracture decreases against the tectonic normal stress magnitude. Among the methods, the shifted power-law method was found to have the widest availability to achieve a high precision. Meanwhile, it was found to be difficult for the Bingham method (Yamaji et al., 2010) to simulate a data distributions having abrupt decreases (Figs. 6b and 6d).

Another advantage of the shifted power-law method is the objective determination of the nondimensionalized fluid pressure with confidence intervals, though the uncertainty was found to be large especially when the shape of distribution is concave. The problem in the method of Jolly and Sanderson (1997) is in the graphical recognition of the angles θ_3 and θ_2 from stereogram (Fig. 6d). It is difficult to determine them objectively without subjectivity.

Commonly to all the methods, the precisions of principal stress axes are sufficient, while those of stress ratios are relatively low. It seems to be difficult

to detect a difference of stress ratio by 0.1. A risk of wrong choice of stochastic model is represented by the test with a step-wise distribution (Section 3.2, Fig. 8), in which the Bingham method almost failed to give the correct stress ratio.

Generally speaking, non-parametric methods have lower precision than parametric ones in return for the exclusion of assumptions on stochastic models. This is of course the case for the present non-parametric method. Although it has lower precisions than the method with the appropriate stochastic model, the level of precision is not unacceptable. Since we should not make an unfounded assumption on natural data, the non-parametric method is worth using.

Yamaji and Sato (2011) extended the model of the Bingham method into the mixed probability distribution in order to detect multiple fracturing events distinguished by stress states. Their method selects the optimal number of stress states by minimizing the index of Bayesian information criterion (BIC, Schwarz, 1978). We applied the method to the dikes in the Tsuruga Bay area. By changing the number of stress states from one to three, the single stress model was found to be optimal (Fig. 12). The homogeneity of the dikes were confirmed at least for the Bingham model. The shifted power-law model can be easily extended to mixed distribution model. However, the non-parametric method is difficult to be improved for multiple events because it does not quantify the frequencies of fractures. The detection of multiple events without a parametric model will be a next methodological challenge.

The analysis of Early Miocene dike swarm in the Tsuruga Bay area suc-

cessfully revealed the stress regime to be normal-faulting. Hoshi and Takagawa (2009) managed to infer the extensional regime by referring to the existence of map-scale NE-SW trending normal faults (Yoshikawa et al., 2002) in the Noto Peninsula located about 200 km to the north of the study area (Fig. 10a). Our result has an importance in that the stress regime was estimated directly from the dikes. Although the dikes in the study area of about 15 km long are compatible with the single stress tensor, the spatial and temporal stability of stress state should be investigated in the future works. In the Noto Peninsula, the tectonic blocks recognized by Kobayashi et al. (2005) are several kilometers in size, and the growth normal faults described by Yoshikawa et al. (2002) imply that the NW-SE trending extensional stress continued from 25 Ma to 19 Ma.

The pore fluid pressure ratio $\lambda' = P_{\mathrm{f}}/P_{\mathrm{l}}$ has a significant effect on the brittle strength of the lithosphere, where P_{l} is the lithostatic (overburden) pressure. It can controls whether the continental rifting is accelerated or not (Takeshita and Yamaji, 1990). Assuming that nearly vertical σ_1 in the Tsuruga Bay area was equal to P_{l}, the nondimensionalized fluid pressure $\lambda \approx 0.76$ determined by the shifted power-law method is the minimum estimate of λ' for the case that $\sigma_3 = 0$. Therefore, the fluid pressure ratio during diking was at least around 0.8. This high level of fluid pressure might have caused the weakening of the lithosphere, which is required for back-arc rifting (Yamasaki and Stephenson, 2011). The problem remained to be solved is how long the high fluid pressure was sustained. Another challenge is the determination of absolute magnitudes of stress and fluid pressure, which seems difficult to achieve only by means of orientation analysis. The shape

and aperture geometry of dilatant fractures (Gudmundsson et al., in press) and fluid inclusions in mineral veins (Andre et al., 2001; Becker et al., 2010) are promising clues to the absolute magnitudes.

Acknowledgments

We are grateful to H. Hoshi for providing information on the outcrops in the Tsuruga Bay area. We also thank S. Ueoka for his support in collecting field data. Comments and suggestions from an anomyous reviewer improved the manuscript.

Appendix A. Frequency of normal stress magnitudes on uniformly distributed fractures

This appendix provides how to calculate the frequency of normal stress magnitudes at uniformly distributed fractures, which is used to draw the histograms of normal stresses in Section 3 and 4.

Eq. (4) says that a contour line of σ_n orthogonally projected from the unit sphere onto the σ_1-σ_2 plane is an ellipse with the major radius of $\sqrt{\sigma_\mathrm{n}/\Phi}$ along σ_2-axis and the minor radius of $\sqrt{\sigma_\mathrm{n}}$ along σ_1-axis (Fig. 13). Then the end points of unit normals to fractures with a constant σ_n can be written as

$$\left\{\begin{array}{rcll} x &=& \sqrt{\sigma_\mathrm{n}}\cos t & \\ y &=& \sqrt{\sigma_\mathrm{n}/\Phi}\sin t & \\ z &=& \sqrt{1-x^2-y^2} & (0 \le t \le 2\pi), \\ &=& \sqrt{1-\sigma_\mathrm{n}\cos^2 t-(\sigma_\mathrm{n}/\Phi)\sin^2 t} & \end{array}\right. \qquad \text{(A.1)}$$

where x, y and z are the coordinates along σ_1-, σ_2- and σ_3-axes, respectively.

Note that when $\sigma_{\mathrm{n}} > \Phi$, the ellipse of Eq. (4) has intersection points with the unit circle $x^2 + y^2 = 1$. For example, the intersection point in the region $x \geq 0, y \geq 0, z \geq 0$ is indicated by

$$t = t_0 = \tan^{-1}\left(\sqrt{\Phi}\sqrt{\frac{1-\sigma_{\mathrm{n}}}{\sigma_{\mathrm{n}}-\Phi}}\right), \tag{A.2}$$

which is illustrated as t_0 in Fig. 13.

The length of contour line for a constant σ_{n} on the unit sphere is obtained by the following integration,

$$L\left(\sigma_{\mathrm{n}}\right) = 8\int_0^{t_1}\sqrt{\left(\frac{\mathrm{d}x}{\mathrm{d}t}\right)^2 + \left(\frac{\mathrm{d}y}{\mathrm{d}t}\right)^2 + \left(\frac{\mathrm{d}z}{\mathrm{d}t}\right)^2}\,\mathrm{d}t, \tag{A.3}$$

where

$$t_1 = \begin{cases} \frac{\pi}{2}\left(\sigma_{\mathrm{n}} \leq \Phi\right) \\ t_0\left(\sigma_{\mathrm{n}} > \Phi\right) \end{cases}. \tag{A.4}$$

To calculate the area on unit sphere in which fracture normals are assigned normal stresses between σ_{n} and $\sigma_{\mathrm{n}} + d\sigma_{\mathrm{n}}$, we need the spatial gradient of σ_{n},

$$\nabla\sigma_{\mathrm{n}} = \left(2x, 2\Phi y, 0\right)^{\mathrm{T}}. \tag{A.5}$$

Then the frequency of uniformly distributed points is proportional to the area:

$$f_{\mathrm{u}}\left(\sigma_{\mathrm{n}}\right) = A\int_0^{t_1}\frac{\frac{\mathrm{d}L}{\mathrm{d}t}}{\left|\nabla\sigma_{\mathrm{n}}\right|\cos\theta}\mathrm{d}t, \tag{A.6}$$

where θ is the angle between $\nabla\sigma_{\mathrm{n}}$ and tangential plane of unit sphere at $\vec{v}$ (Fig. 13), and A is the normalizing factor to make f_{u} a probability density.

Since the integration in Eq. (A.6) cannot be calculated analytically, we employed numerical integration. Fig. 14 shows the frequency for various values of Φ.

References

Anderson, E. M., 1951. The dynamics of faulting and dyke formation with application to Britain, 2nd Edition. Oliver and Boyd, Edinburgh.

André, A. S., Sausse, J., Lespinasse, M., 2001. New approach for the quantification of paleostress magnitudes: application to the Soultz vein system (Rhine graben, France). Tectonophysics 336 (1-4), 215–231.

Angelier, J., 1989. From orientation to magnitudes in paleostress determinations using fault slip data. Journal of Structural Geology 11 (1-2), 37–50.

Becker, S., Eichhubl, P., Laubach, S., Reed, R., Lander, R., Bodnar, R., Mar. 2010. A 48 m.y. history of fracture opening, temperature, and fluid pressure: Cretaceous Travis Peak Formation, East Texas basin. Geological Society of America Bulletin 122 (7-8), 1081–1093.

Bingham, C., 1974. An antipodally symmetric distribution on sphere. Annals of Statistics 2 (6), 1201–1225.

Delaney, P. T., Pollard, D. D., Ziony, J. I., Mckee, E. H., 1986. Field relations between dikes and joints: Emplacement processes and paleostress analysis. Journal of Geophysical Research-Solid Earth and Planets 91 (B5), 4920–4938.

Fisher, F., 1953. Dispersion on a sphere. Proceedings of the Royal Society of London A217, 295–305.

Gudmundsson, A., Kusumoto, S., Simmenes, T. H., Philipp, S. L., Larsen,

B., Lotveit, I. F., in press. Effects of overpressure variations on fracture apertures and fluid transport. Tectonophysics.

Hoshi, H., Takagawa, M., 2009. Early Miocene parallel dike swarms in the Tsuruga Bay area, back-arc side of central Japan. Journal of the Geological Society of Japan 115 (2), 96–99.

Jolly, R. J. H., Sanderson, D. J., 1997. A Mohr circle construction for the opening of a pre-existing fracture. Journal of Structural Geology 19 (6), 887–892.

Kobayashi, H., Yamaji, A., Masuda, F., 2005. Miocene stratigraphy, sedimentary environments and tectonics in the Wajima area, Noto Peninsula, southern margin of the Japan Sea. Journal of Geological Society of Japan 111 (5), 286–299 (in Japanese with English abstract).

Mazzarini, F., Isola, I., 2007. Hydraulic connection and fluid overpressure in upper crustal rocks: Evidence from the geometry and spatial distribution of veins at botrona quarry, southern tuscany, italy. Journal of Structural Geology 29 (8), 1386–1399.

Nakamura, K., 1977. Volcanos as possible indicators of tectonic stress orientation - principle and proposal. Journal of Volcanology and Geothermal Research 2 (1), 1–16.

Nelder, J. A., Mead, R., 1965. A simplex method for function minimization. The Computer Journal 7 (4), 308–313.

Orife, T., Lisle, R. J., 2003. Numerical processing of palaeostress results. Journal of Structural Geology 25 (6), 949–957.

Rakhmanov, E. A., Saff, E. B., Zhou, Y. M., 1994. Minimal discrete energy on the sphere. Mathematical Research Letters 1 (6), 647–662.

Scheidegger, A. E., 1965. On the statistics of the orientation of bedding planes, grain axes, and similar sedimentological data. United States Geological Survey Professional Paper 525-C, 164–167.

Schwarz, G., 1978. Estimating the dimension of a model. The Annals of Statistics 6 (2), 461–464.

Spearman, C., 1904. The proof and measurement of association between two things. American Journal of Psychology 15 (1), 72–101.

Takeshita, T., Yamaji, A., 1990. Acceleration of continental rifting due to a thermomechanical instability. Tectonophysics 181 (1-4), 307–320.

Wakita, K., Harayama, S., Kano, K., Mimura, K., Sakamoto, T., Hiroshima, T., Komazawa, M., 1992. Geological map of Japan 1:200,000, Gifu. Geological Survey of Japan.

Woodcock, N. H., 1977. Specification of fabric shapes using an eigenvalue method. Geological Society of America Bulletin 88, 231–1236.

Yamaji, A., Sato, K., 2006. Distances for the solutions of stress tensor inversion in relation to misfit angles that accompany the solutions. Geophysical Journal International 167 (2), 933–942.

Yamaji, A., Sato, K., 2011. Clustering of fracture orientations using a mixed Bingham distribution and its application to paleostress analysis from dike or vein orientations. Journal of Structural Geology 33 (7), 1148 – 1157.

Yamaji, A., Sato, K., Tonai, S., 2010. Stochastic modeling for the stress inversion of vein orientations: Paleostress analysis of Pliocene epithermal veins in southwestern Kyushu, Japan. Journal of Structural Geology 32 (8), 1137–1146.

Yamasaki, T., Stephenson, R., 2011. Back-arc rifting initiated with a hot and wet continental lithosphere. Earth and Planetary Science Letters 302 (1-2), 172–184.

Yoshikawa, T., Kano, K., Yanagisawa, Y., Komazawa, M., Joshima, M., Kikawa, E., 2002. Geology of the Suzumisaki, Noto-iida and Horyuzan District, Quadrangle Series, 1:50000. Geological Survey of Japan, AIST (in Japanese).

Figure captions

Figure 1

A schematic drawing of dilatant fractures in a rock mass. In a uniform and constant stress state symbolized by σ_1-, σ_2- and σ_3-axes, a dilatant fracture occurs if the fluid pressure P_f exceeds the tectonic normal stress σ_n. The shear stress τ and normal stress σ_n depend on the orientation of fracture described by the unit normal vector v.

Figure 2

Orientational distribution of normal stress magnitude for various values of stress ratio Φ. Lower-hemisphere and equal-area projection. Gray scale colors at poles of fractures indicate normalized magnitude of normal stress ($0 \leq \sigma_\mathrm{n} \leq 1$). The principal stress magnitudes are normalized as $\sigma_1 = 1$ and $\sigma_3 = 0$.

Figure 3

Schematic figures to explain the aim of this study. σ_1, σ_2 and σ_3 are principal stresses. σ_n and τ denotes normal and shear stresses. (a) Jolly and Sanderson (1997) suggested that the orientations of fractures to be dilated are restricted by the fluid pressure (P_f) within the shaded regions in the stereogram indicating fracture poles and the Mohr's diagram. They did not mentioned about the difference of frequency within the feasible range. (b) Yamaji et al. (2010) modified the Jolly and Sanderson's method to express the monotonically-decreasing feature of fracture frequency against the increase of tectonic normal stress acting on the fracture surface by utilizing Bingham type of stochastic model. Grayscale colors indicate the frequency of

fractures. (c) This study intends to test the validity of the stochastic model and proposes modified methods to deal with various types of frequency distributions.

Figure 4

Various shapes of shifted power-law distribution without normalization as probability density. The values in boxes are the exponents n in Eq. (9).

Figure 5

A schematic figure to explain how to calculate the rank correlation coefficient. (a) Open circles are grid points uniformly distributed on the unit sphere. Small dots are observed fracture poles, of which frequency distribution is shown by the contour lines (gray solid lines). The italic numbers attached on the grid points are the ranks according the frequency in descending order. σ_3-axis is of an arbitrary chosen reduced stress tensor. The bold numbers are the ranks of the grid points according to the normal stress magnitude in ascending order (the smallest around σ_3-axis). (b) Correlation chart for the fracture frequency and the normal stress magnitude. Spearman's rank correlation coefficient does not assume this scattered points to lie on a straight line so as Peason's correlation coefficient does. Only the correspondence between the orders of points along horizontal and vertical axes are evaluated.

Figure 6

Fracture orientation datasets analyzed in this study. Small dots are the fracture poles plotted in stereograms in lower-hemisphere and equal area

projections. Their densities are also visualized as grayscale contour lines. Large circle, diamond and square symbols are the principal stress axes. (a) Data obeying a Bingham distribution with $\kappa_1 = -6$ and $\kappa_2 = -3$, i.e., $\Phi = 0.5$. (b) Data obeying a step-wise frequency distribution which has $\lambda = 0.6$, $n = 0$ and $\Phi = 0.3$ when expressed as a shifted power-law function. (c) Data from the quartz vein swarm from Hashima area, southern Japan. (d) Data from the andesitic dike swarm from the Tsuruga Bay area, central Japan. A stress solution by the method of Jolly and Sanderson (1997), of which stress ratio is $\Phi = 0.67$, is superimposed.

Figure 7

The results of analyses of an artificial data (Fig. 6a) obeying a Bingham distribution. Left, middle and right columns corresponds to the Bingham method, the shifted power-law method and the non-parametric method. (a) Principal stress axes of the optimal solutions with 95% confidence regions defined by 950 bootstrap solutions. Large open symbols (circles, diamonds and squares) are of the optimal solutions and tiny ones are of the bootstrap solutions which broken lines enclose. Small black dots are the fracture poles analyzed. (b) The other parameters determined in the analyses; κ_1 and κ_2 for the Bingham method, n and λ for the shifted power-law method and the stress ratio Φ for all the three methods. Black diamonds are the optimal solutions and broken lines indicate the assumed solutions. The histograms show the distributions of bootstrap solutions within the 95% confidence intervals. (c) Normal stress magnitudes on fracture surfaces calculated according to the optimal stresses. The first row includes Mohr's diagrams where open circles indicate normal and shear stress magnitudes on the fractures. The second

row shows the corrected frequency histograms of normal stress magnitudes and optimized distribution functions (bold lines with parameters shown in the formulas $f_{\mathrm{B}}(\kappa_1, \kappa_2, \Phi)$ and $f_{\mathrm{p}}(n, \lambda, \Phi)$). See text and Appendix A for the details about correction.

Figure 8

The results of analyses of an artificial data (Fig. 6b) obeying a step-wise distribution. Charts and symbols are similar to those of Fig. 7.

Figure 9

The results of analyses of the quartz vein swarm in the Hashima area, southern Japan. The data measured by Yamaji et al. (2010) is shown in Fig. 6c. Charts and symbols are similar to those of Fig. 7.

Figure 10

(a) Geologic map of the Tsuruga Bay area (simplified from Wakita et al., 1992). (b) A dike intruded into mélange of the Mino accretionary complex. (c) A jigsaw structure showing the opening direction perpendicular to the general trend of dike.

Figure 11

The results of analyses of the andesitic dike swarm in the Tsuruga Bay area, central Japan. Charts and symbols are similar to those of Fig. 7.

Figure 12

BIC indices obtained by the mixed Bingham distribution analysis (Yamaji and Sato, 2011) applied to the dikes in the Tsuruga Bay area. The smallest

index was achieved by the single stress model, showing the homogeneity of the data.

Figure 13

Schematic figure showing the isovalue lines with respect to normal stress magnitude on unit sphere. Grayscale colors indicates normal stress magnitudes. Only the first octant ($x \geq 0$, $y \geq 0$, $z \geq 0$) is drawn for the orthogonal symmetry. See Appendix A for explanation of values on this figure.

Figure 14

Isovalue area on unit sphere with respect to normal stress magnitude σ_{n}, which are normalized as probability densities. Numbers in boxes are values of stress ratio Φ.

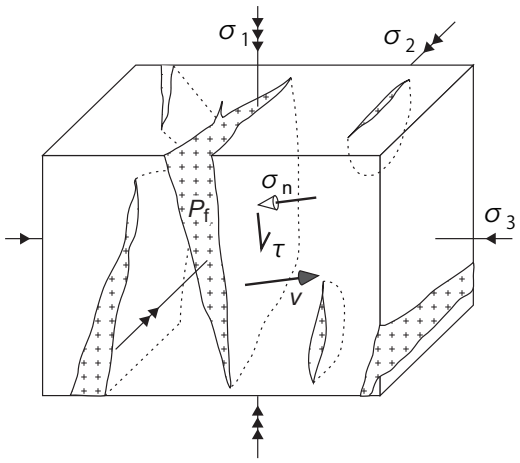

Figure 1: Sato et al.

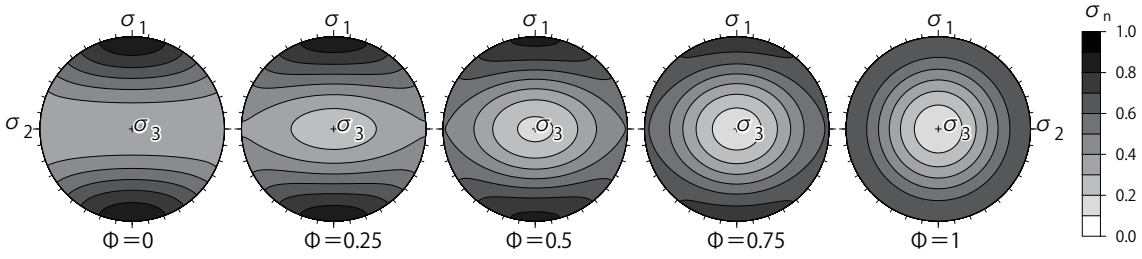

Figure 2: Sato et al.

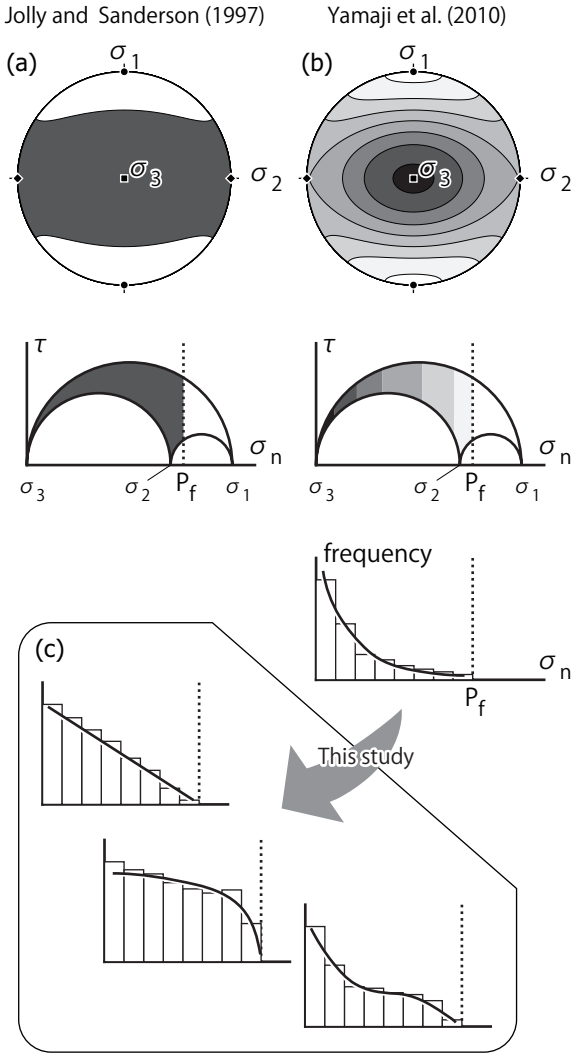

Figure 3: Sato et al.

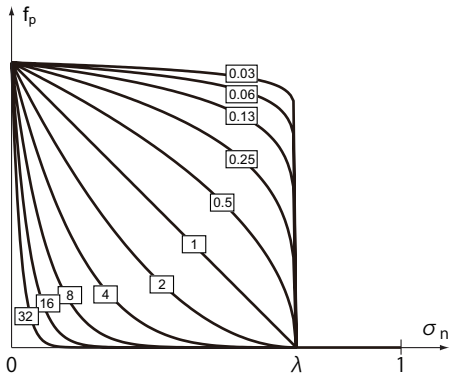

Figure 4: Sato et al.

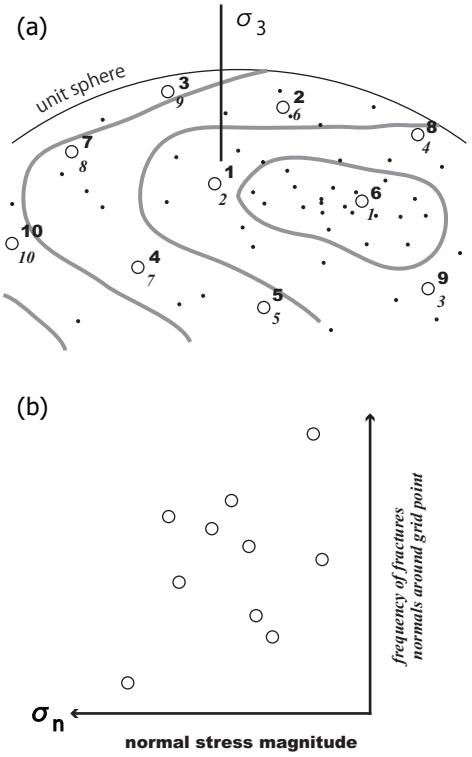

Figure 5: Sato et al.

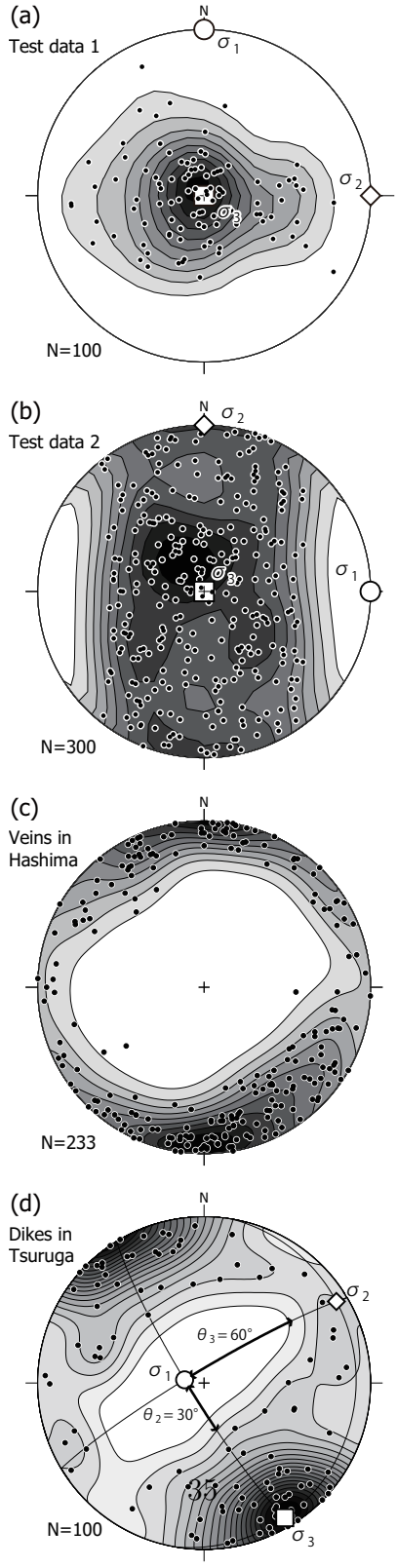

Figure 6: Sato et al.

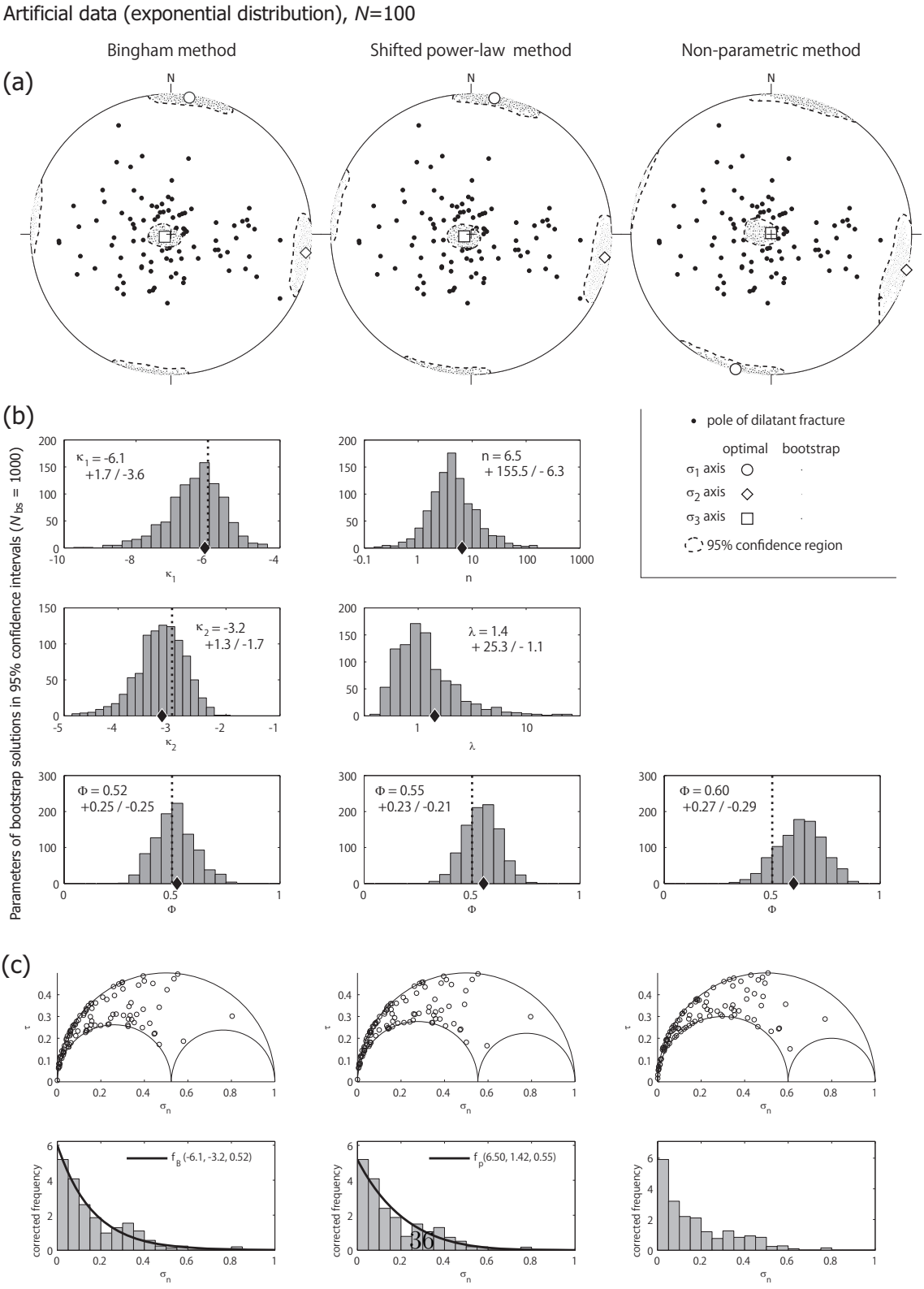

Figure 7: Sato et al.

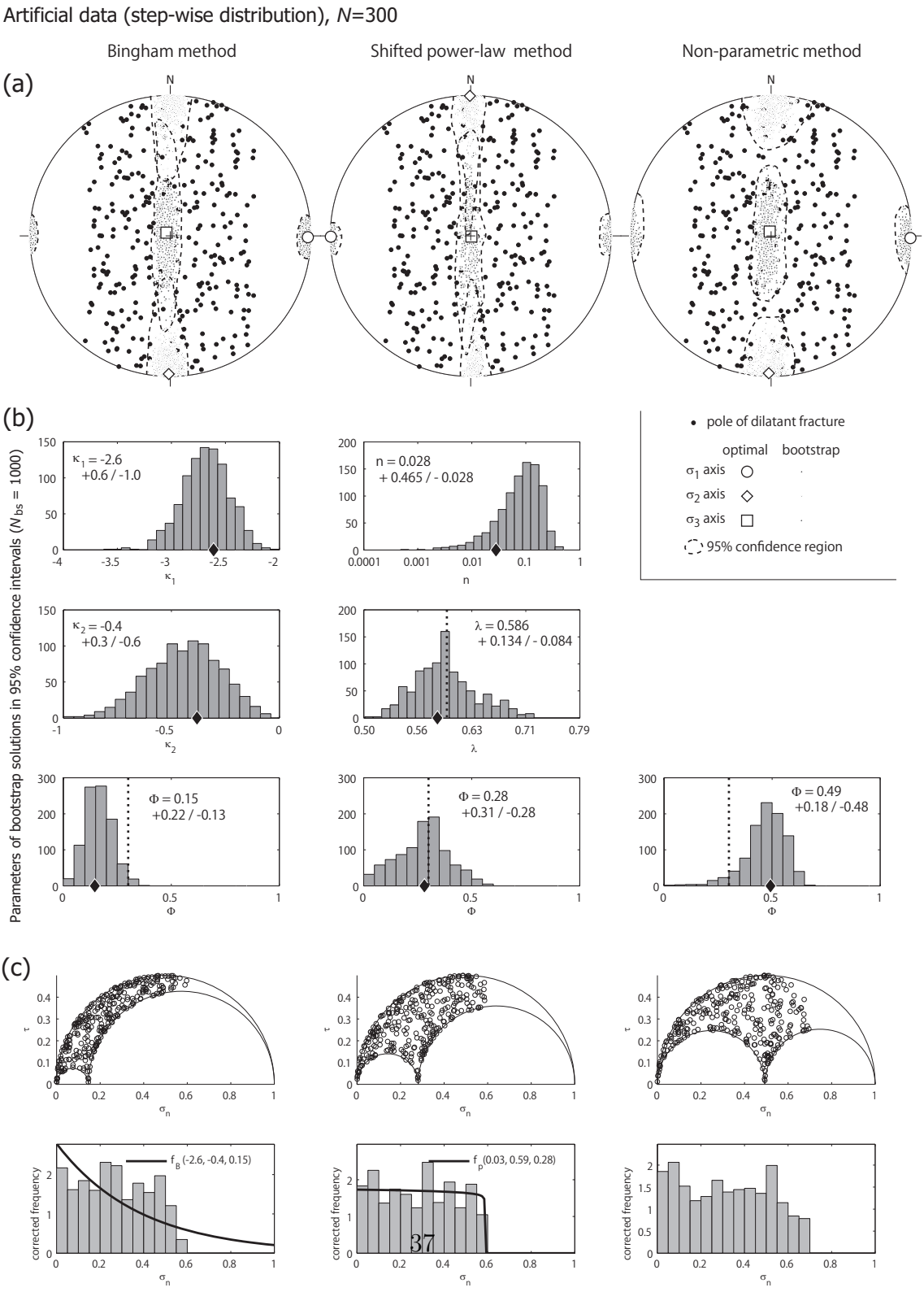

Figure 8: Sato et al.

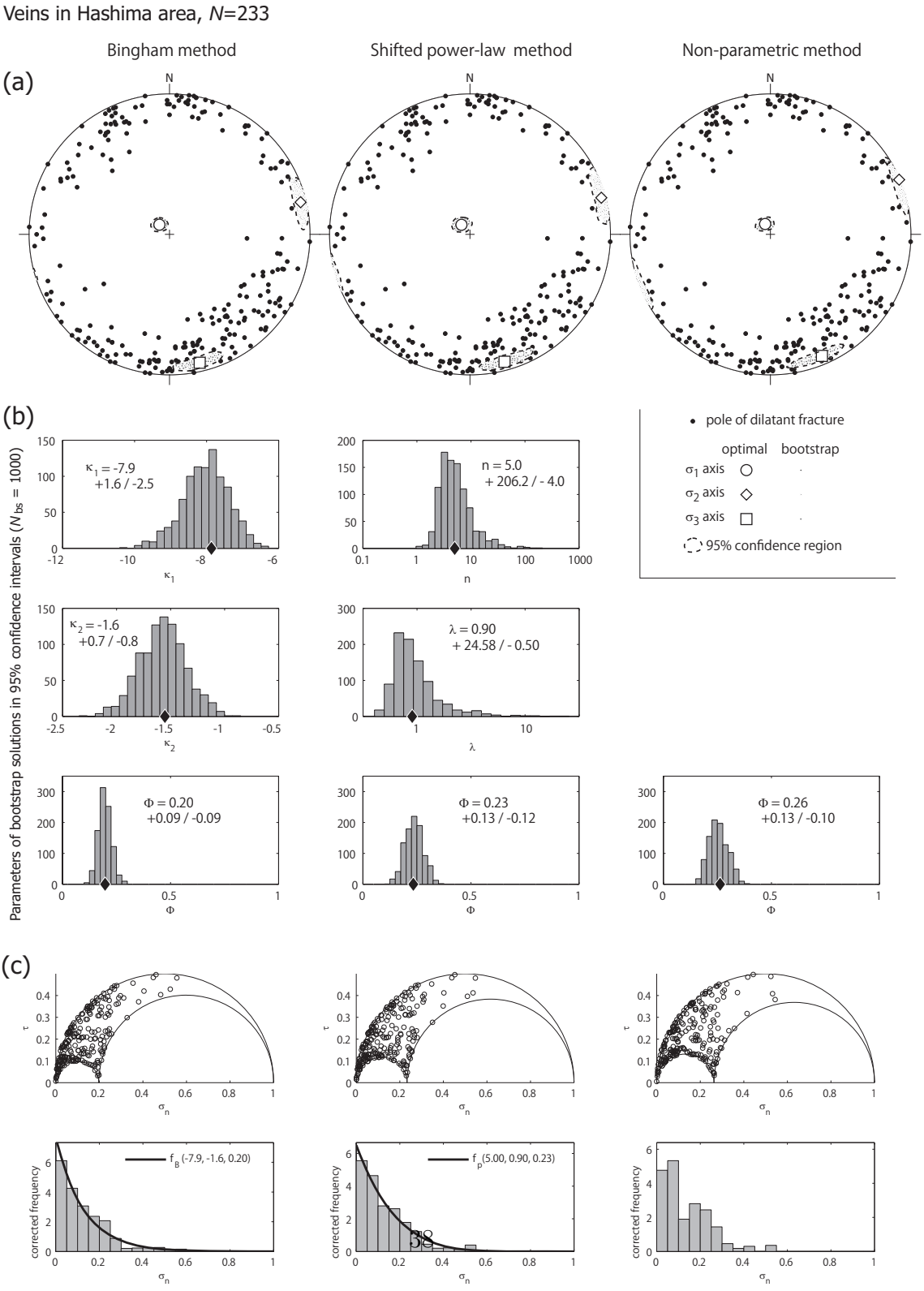

Figure 9: Sato et al.

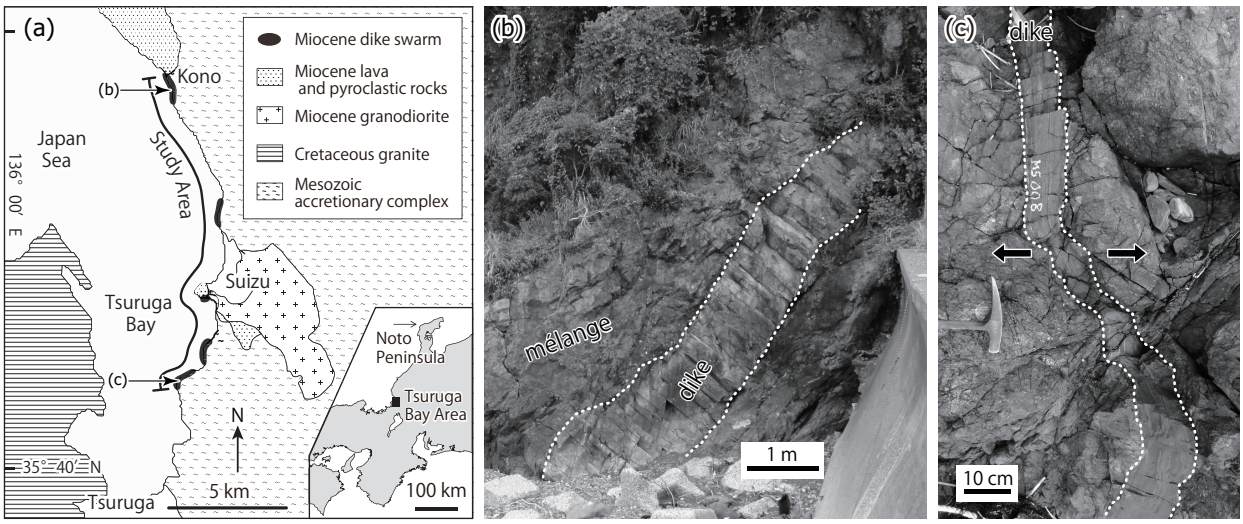

Figure 10: Sato et al.

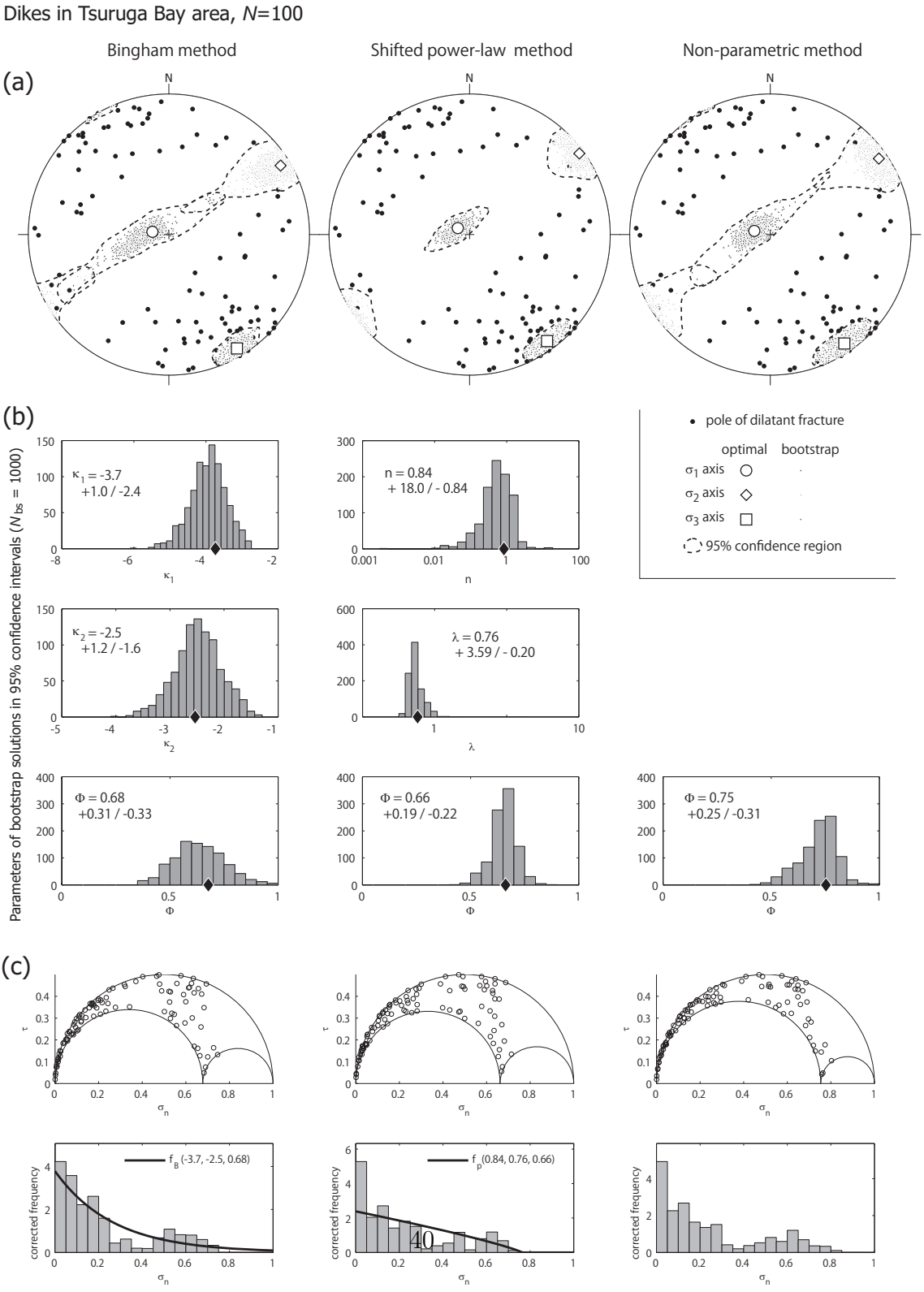

Figure 11: Sato et al.

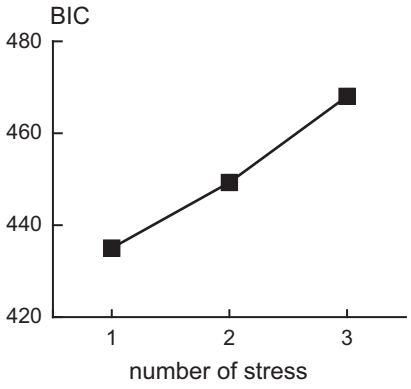

Figure 12: Sato et al.

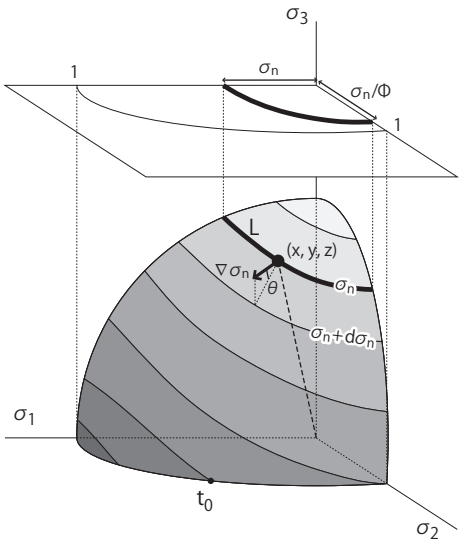

Figure 13: Sato et al.

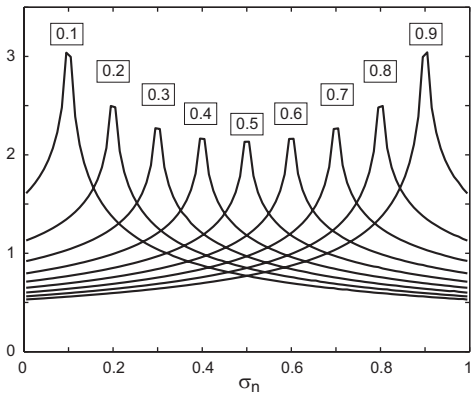

Figure 14: Sato et al.